LIDAR-Aided Inertial Navigation with Extended Kalman Filtering for Pinpoint Landing

David M. Busnardo[1], Matthew L. Aitken[2], and Robert H. Tolson[3]
North Carolina State University, Raleigh, NC 27695

Diego Pierrottet[4]
Coherent Applications, Inc., Hampton, VA 23666

and
Farzin Amzajerdian[5]
NASA Langley Research Center, Hampton, VA 23681

In support of NASA's Autonomous Landing and Hazard Avoidance Technology (ALHAT) project, an extended Kalman filter routine has been developed for estimating the position, velocity, and attitude of a spacecraft during the landing phase of a planetary mission. The proposed filter combines measurements of acceleration and angular velocity from an inertial measurement unit (IMU) with range and Doppler velocity observations from an onboard light detection and ranging (LIDAR) system. These high-precision LIDAR measurements of distance to the ground and approach velocity will enable both robotic and manned vehicles to land safely and precisely at scientifically interesting sites. The filter has been extensively tested using a lunar landing simulation and shown to improve navigation over flat surfaces or rough terrain. Experimental results from a helicopter flight test performed at NASA Dryden in August 2008 demonstrate that LIDAR can be employed to significantly improve navigation based exclusively on IMU integration.

Nomenclature

A	=	direction cosine matrix rotating from navigation frame to vehicle body frame
$\boldsymbol{a}$	=	net body acceleration, m/s^2
$\boldsymbol{a}_m$	=	measured net body acceleration, m/s^2
$\boldsymbol{b}_a$	=	accelerometer drift-rate bias, m/s^2
$\boldsymbol{b}_g$	=	gyroscope drift-rate bias, rad/s
$\boldsymbol{g}$	=	gravitational acceleration, m/s^2
$\boldsymbol{l}_i$	=	direction cosines of the *i*-th LIDAR beam in the vehicle body frame
$\boldsymbol{n}_a$	=	accelerometer drift-rate noise, m/s^2
$\boldsymbol{n}_g$	=	gyroscope drift-rate noise, rad/s
$\boldsymbol{n}_{ra}$	=	accelerometer drift-rate ramp noise, m/s^3
$\boldsymbol{n}_{rg}$	=	gyroscope drift-rate ramp noise, rad/s^2

[1]NCSU Graduate Research Assistant, National Institute of Aerospace, 100 Exploration Way, Hampton, VA 23666
[2]NCSU Graduate Research Assistant, National Institute of Aerospace, 100 Exploration Way, Hampton, VA 23666, AIAA Student Member
[3]NCSU Langley Professor, National Institute of Aerospace, 100 Exploration Way, Hampton, VA 23666, AIAA Associate Member
[4]Coherent Applications, Inc., 20 Research Dr., Hampton, VA 23666
[5]Senior Research Scientist. NASA Langley Research Center, MS 468, Hampton, VA 23681

$\boldsymbol{p}$	=	position, m
q	=	attitude quaternion corresponding to A
$\boldsymbol{v}$	=	velocity, m/s
$\boldsymbol{x}$	=	state vector
$\hat{\boldsymbol{x}}$	=	state estimate
$\tilde{\boldsymbol{x}}$	=	reduced-dimension state vector
$\boldsymbol{z}$	=	measurement vector
$\Delta\tilde{\boldsymbol{x}}$	=	reduced-dimension state error vector
δq	=	quaternion error
$\delta\boldsymbol{\theta}$	=	infinitesimal attitude error angle vector
Π	=	projection matrix [0 0 1]
ρ	=	range (distance to the ground), m
$\dot{\rho}$	=	Doppler (line-of-sight) velocity, m/s
$\boldsymbol{\omega}$	=	body angular velocity, rad/s
$\boldsymbol{\omega}_e$	=	angular velocity of the Earth, rad/s
$\boldsymbol{\omega}_m$	=	measured body angular velocity, rad/s

I. Introduction

FUTURE space exploration will require that descent vehicles employ accurate real-time state estimation, providing the capability to land precisely and safely at scientifically promising but potentially hazardous sites. Robotic exploration, sample return, and human missions to the Moon, Mars, and other bodies in the solar system warrant the development of sophisticated hazard avoidance and precision landing technologies. Pinpoint landing will be particularly vital for human exploration vehicles, which will need to land proximate to pre-positioned supplies and emergency abort systems.

For this reason, the development of a more capable and robust landing system, featuring a LIDAR-based autonomous guidance and control instrument, is essential for reducing risks and increasing performance of future planetary missions. The flight-qualified version of this technology is anticipated to have the capability of navigating to within 10 to 100 m of the target by analyzing terrain features and identifying safe landing sites [1]. Moreover, the system will provide real-time trajectory updates, in particular surface proximity, orientation, and vector velocity [2]. Two laser sensors are employed to meet these objectives: a three-dimensional imaging LIDAR to provide surface topography information and a coherent range and velocity LIDAR to provide precision altitude, velocity, and attitude updates. Demonstrating the ability of the range and velocity LIDAR to estimate the state of the vehicle is the subject of this report.

To accomplish this task, an extended Kalman filter (EKF) has been developed to estimate position, velocity, and attitude during landing. The proposed estimator combines measurements of acceleration and angular velocity from an IMU with range and Doppler velocity observations from an onboard LIDAR system. Pseudo-data generated for a lunar landing simulation was used to test the filter's performance, using trajectories over flat surfaces, "rocky" terrain, and "hilly" terrain. Data from a helicopter flight test carried out at NASA Dryden in August 2008 was used to evaluate true system performance over smooth terrain. Analysis of the results shows filter estimates in excellent agreement with high-accuracy GPS measurements.

II. Sensor Models

Even the most advanced inertial navigation systems suffer from misalignment, bias, and integration drift; by themselves, accelerometers and gyroscopes provide changes to the state with ever-increasing error. For this reason, IMU data is often combined with external measurements to improve navigation accuracy. Specifically, this report examines the use of LIDAR range and Doppler velocity observations in supplementing the measurements provided by the IMU.

A. Inertial Measurement Unit

Following [4], both the accelerometer and gyroscope are assumed to be corrupted by a drift-rate bias and drift-rate noise, the latter of which is modeled as a Gaussian white noise process. Thus, the sensor outputs are given by

$$\boldsymbol{a}_m = A(\boldsymbol{a} - \boldsymbol{g}) + \boldsymbol{b}_a + \boldsymbol{n}_a \qquad \boldsymbol{\omega}_m = A\boldsymbol{\omega} + \boldsymbol{b}_g + \boldsymbol{n}_g$$

The drift-rate biases are not constant, but are instead driven by drift-rate ramp noise

$$\frac{\mathrm{d}}{\mathrm{d}t}\boldsymbol{b}_a = \boldsymbol{n}_{ra} \qquad \frac{\mathrm{d}}{\mathrm{d}t}\boldsymbol{b}_g = \boldsymbol{n}_{rg}$$

where $\boldsymbol{n}_{ra}$ and $\boldsymbol{n}_{rg}$ are assumed to be Gaussian white noise processes. IMU data are not treated as observations, and thus IMU noise appears as state noise instead of observation noise.

B. LIDAR System

In addition to the IMU, the vehicle is also equipped with a LIDAR system containing a single emitter and three receivers, each of which directs a laser beam, directed at a polar angle of 22.5° from the body's negative z-axis; moreover, the three beams are separated azimuthally from each other by angles of 120° (see Fig. 1) [3]. Each LIDAR signal measures distance to the ground (range) and line-of-sight velocity. Thus, the measurement vector, which is understood to be in the vehicle body coordinate system, is given by

$$\boldsymbol{z} = \begin{bmatrix} \rho_1 & \rho_2 & \rho_3 & \dot{\rho}_1 & \dot{\rho}_2 & \dot{\rho}_3 \end{bmatrix}^T = \begin{bmatrix} \boldsymbol{\rho}^T & \dot{\boldsymbol{\rho}}^T \end{bmatrix}^T \tag{1}$$

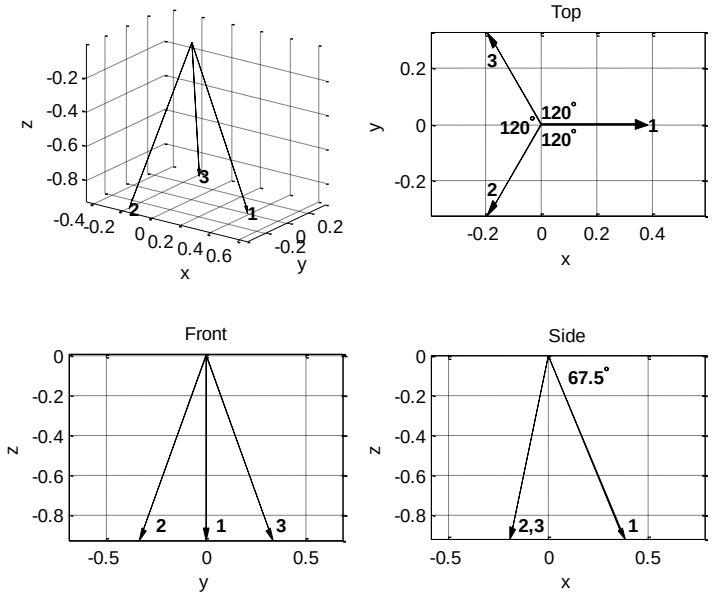

Fig. 1 LIDAR system geometry

III. Estimator Description

The standard EKF equations for propagating and updating the state estimate can be found in [5,6]. Presented here are highlights of the state equation, in addition to error and measurement models.

A. The State Equation

The state of the vehicle consists of the position, velocity, attitude quaternion, and two drift-rate bias vectors

$$\boldsymbol{x} = \begin{bmatrix} \boldsymbol{p} & \boldsymbol{v} & \boldsymbol{b}_a & q & \boldsymbol{b}_g \end{bmatrix}^T$$

and thus has dimension 16. Here, $\boldsymbol{p}$ and $\boldsymbol{v}$ are understood to be in the navigation frame, while $\boldsymbol{b}_a$ and $\boldsymbol{b}_g$ are understood to be in the vehicle body frame. With time derivatives taken with respect to the navigation coordinate system—assumed here to be planet-fixed and rotating—the kinematic equations can be formulated as a first-order system of differential equations [6,7]

$$\dot{\boldsymbol{x}} = \begin{bmatrix} \dot{\boldsymbol{p}} \\ \dot{\boldsymbol{v}} \\ \dot{\boldsymbol{b}}_a \\ \dot{q} \\ \dot{\boldsymbol{b}}_g \end{bmatrix} = \begin{bmatrix} \boldsymbol{v} \\ \boldsymbol{a} - 2[\boldsymbol{\omega}_e \times]\boldsymbol{v} - [\boldsymbol{\omega}_e \times]^2 \boldsymbol{p} \\ \boldsymbol{n}_{ra} \\ \tfrac{1}{2}\Omega\big(A(\boldsymbol{\omega} - \boldsymbol{\omega}_e)\big)q \\ \boldsymbol{n}_{rg} \end{bmatrix} = \begin{bmatrix} \boldsymbol{v} \\ A^T(\boldsymbol{a}_m - \boldsymbol{b}_a - \boldsymbol{n}_a) + \boldsymbol{g} - 2[\boldsymbol{\omega}_e \times]\boldsymbol{v} - [\boldsymbol{\omega}_e \times]^2 \boldsymbol{p} \\ \boldsymbol{n}_{ra} \\ \tfrac{1}{2}\Omega(\boldsymbol{\omega}_m - \boldsymbol{b}_g - \boldsymbol{n}_g - A\boldsymbol{\omega}_e)q \\ \boldsymbol{n}_{rg} \end{bmatrix} \tag{2}$$

B. State Error Model

Following [5], the elements of the state error vector are given by the difference between true and estimated quantities, with the exception of the quaternion error. Due to the constraint on the quaternion norm, a standard additive error model for the quaternion would result in a singular covariance matrix. One way to avoid this singularity is to represent the full covariance matrix by a matrix of smaller dimension. Consequently, the true quaternion is modeled as the product of the quaternion error and the estimated quaternion

$$q = \delta q \otimes \hat{q} \Leftrightarrow \delta q = q \otimes \hat{q}^{-1}$$

Since the infinitesimal attitude error corresponds to a small rotation angle, the following small angle approximation can be applied $\delta q \approx \begin{bmatrix} \delta \boldsymbol{q} \\ 1 \end{bmatrix} = \begin{bmatrix} \frac{1}{2}\delta\boldsymbol{\theta} \\ 1 \end{bmatrix}$

and hence, the attitude error information is fully contained within the 3×1 tilt angle vector $\delta\boldsymbol{\theta}$. The uncertainty in the attitude estimate is thus characterized by a 3×3 covariance matrix of full rank.

Writing the reduced-dimension state vector $\tilde{\boldsymbol{x}} = \begin{bmatrix} \boldsymbol{p} & \boldsymbol{v} & \boldsymbol{b}_a & \delta\boldsymbol{\theta} & \boldsymbol{b}_g \end{bmatrix}^T$

and its corresponding predicted value (noting that the expectation value of $\delta\boldsymbol{\theta}$ is a 3×1 null vector)

$$\hat{\tilde{\boldsymbol{x}}} = \begin{bmatrix} \hat{\boldsymbol{p}} & \hat{\boldsymbol{v}} & \hat{\boldsymbol{b}}_a & \boldsymbol{0} & \hat{\boldsymbol{b}}_g \end{bmatrix}^T$$

the reduced-dimension state error vector is given by $\Delta\tilde{\boldsymbol{x}} = \tilde{\boldsymbol{x}} - \hat{\tilde{\boldsymbol{x}}} = \begin{bmatrix} \Delta\boldsymbol{p} & \Delta\boldsymbol{v} & \Delta\boldsymbol{b}_a & \delta\boldsymbol{\theta} & \Delta\boldsymbol{b}_g \end{bmatrix}^T$.

C. Measurement Sensitivity Matrix

Assuming that the landing surface is flat and that the navigation *z*-axis is normal to this surface, the relationship

$$\Pi\boldsymbol{p} + \rho_i(\Pi A^T \boldsymbol{l}_i) = 0 \qquad i = 1, 2, 3 \tag{3}$$

is satisfied. From Eq. (3), it follows that

$$\left.\frac{\partial \rho_i}{\partial \boldsymbol{p}}\right|_{\hat{\tilde{\boldsymbol{x}}}} = \frac{-\Pi}{\Pi \hat{A}^T \boldsymbol{l}_i} \tag{4}$$

and

$$\left.\frac{\partial \rho_i}{\partial \delta\boldsymbol{\theta}}\right|_{\hat{\tilde{\boldsymbol{x}}}} = -\Pi\hat{\boldsymbol{p}}(\Pi\hat{A}^T\boldsymbol{l}_i)^{-2}\Pi\hat{A}^T[\boldsymbol{l}_i\times] \tag{5}$$

The partial derivatives of range with respect to the other state variables are trivially zero.

Regardless of the surface topography, each Doppler velocity measurement is simply the component of the spacecraft velocity along the respective LIDAR direction

$$\dot{\rho}_i = (A^T\boldsymbol{l}_i)\cdot\boldsymbol{v} = (A^T\boldsymbol{l}_i)^T\boldsymbol{v} = \boldsymbol{l}_i^T A\boldsymbol{v} \qquad i = 1, 2, 3 \tag{6}$$

Using the notation from Eq. (1), and defining the matrix $L = \begin{bmatrix} \boldsymbol{l}_1 & \boldsymbol{l}_2 & \boldsymbol{l}_3 \end{bmatrix}$

Eq. (6) is more compactly written $\dot{\boldsymbol{\rho}} = L^T A\boldsymbol{v}$ from which it follows that

$$\left.\frac{\partial \dot{\boldsymbol{\rho}}}{\partial \boldsymbol{v}}\right|_{\hat{\tilde{\boldsymbol{x}}}} = L^T\hat{A} \tag{7}$$

and

$$\left.\frac{\partial \dot{\boldsymbol{\rho}}}{\partial \delta\boldsymbol{\theta}}\right|_{\hat{\tilde{\boldsymbol{x}}}} = L^T[(\hat{A}\hat{\boldsymbol{v}})\times] \tag{8}$$

The partials with respect to the other state variables vanish, and the measurement sensitivity matrix, then, is easily formed using Eqs. (4), (5), (7), and (8).

IV. Simulation Results

The filter was tested using a lunar landing simulation to analyze the response of the filter to various terrains. Initial tuning was based on a flat surface. Simulations were performed to evaluate the performance over terrains including hemispherical bumps and sine wave hills.

A. Flat Surface

Several studies were conducted using the original filter to explore how changes in the LIDAR beam geometry or limited data would influence the estimate of the state for trajectories over a flat surface. These studies included varying the polar angle of the LIDAR beams from the current 22.5°, including small misalignments in the beam directions, and limiting the gathered LIDAR data to only range or Doppler measurements. In this simulation, the surface is assumed to be at an altitude of 0m. The navigation z-axis is normal to the surface and directed upward. The x-axis is an arbitrary direction in the surface of the plane, and the y-axis completes the right-hand coordinate system. The navigation coordinate system is taken to be inertial; that is, the rotation of the planet was ignored. The IMU axes are assumed identical to that of the vehicle body coordinate system.

Planetary gravitational acceleration is a constant g = 1.625 m/s^2, and acts opposite the navigation z-axis. The simulation initial conditions were taken as follows: altitude = 337 m, velocity = 20.2 m/s, flight path angle 0°, yaw = 45°, pitch = -14° and roll = 0°. The vehicle experiences a constant thrust of 0.98g along the body z-axis, and a constant pitch rate of 0.002443 rad/s. These conditions were selected so that the spacecraft would land upright on the surface with no x- or y-velocity, and minimal z-velocity. In this simulation, the initial estimate of the state was chosen to vary from the true state. The initial position error is 100m in all directions, while the initial velocity error was selected to be 5m/s in all directions. The yaw, pitch, and roll vary from the true state by -3, 5, and 5 degrees respectively. The accelerometer and gyro biases were initially estimated at zero. Fig. 2, below, shows an overhead view of the trajectory with the x-y ground tracks of the LIDAR beams. The circles along the ground tracks are placed every ten seconds, as a visual representation of the velocity.

First, the polar angle of the LIDAR beams was varied between 10° and 50° to determine if the current 22.5° was adequate in estimating the spacecraft state. Fig. 3 shows the errors in the estimated state for polar angles of 10°, 30°, and 50°.

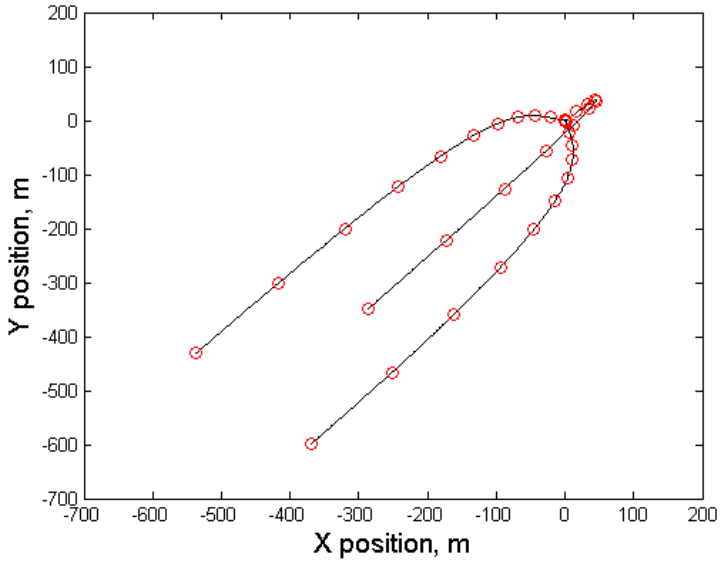

Fig. 2 LIDAR ground tracks for simulated trajectory

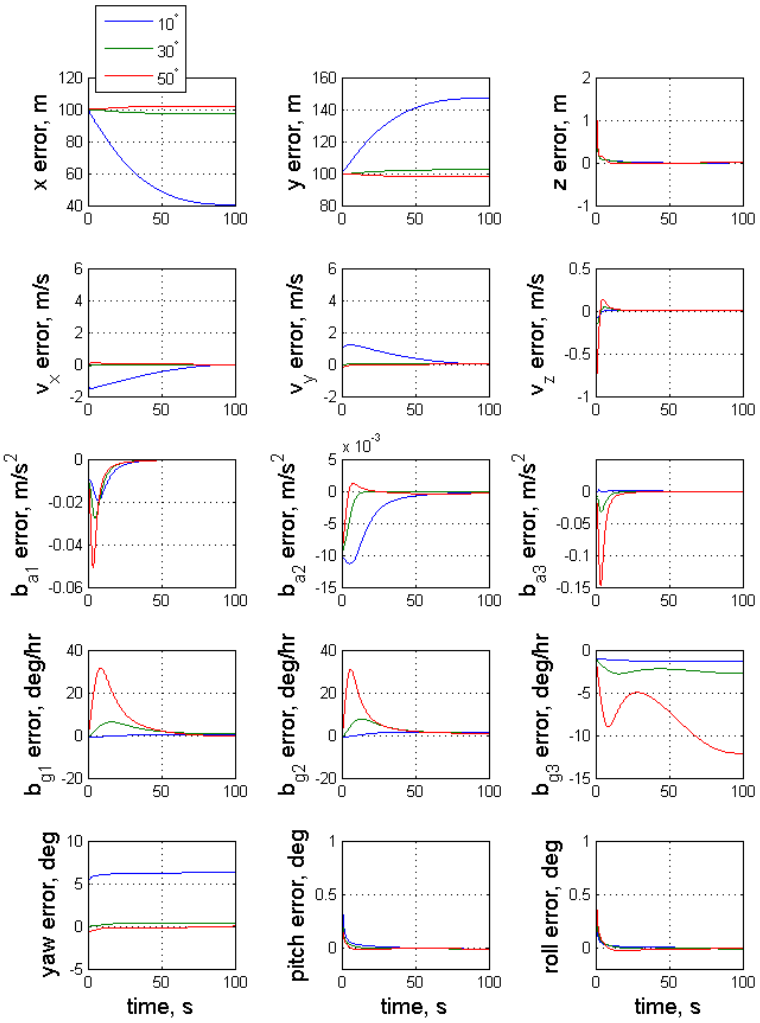

Fig. 3 Errors in estimated state for varying LIDAR polar angles

For small polar angles such as 10-15°, the filter estimates altitude and vertical velocity well, at the expense of the x and y directions. Note that the x and y position and velocity estimates diverge in opposite directions. This is primarily due to the 45° angle of the trajectory in the x-y plane. Accelerometer and gyro biases are also generally better estimated. With larger polar angles of 40-50°, the filter is slower in refining estimates of altitude and vertical velocity, but estimates in other directions are significantly improved. However, the accelerometer and gyro biases are not as well estimated. For orientation estimates, larger polar angles result in better estimates, but differences are not significant in pitch and roll. Based on these results, the current beam geometry with a polar angle of 22.5° is a good compromise that avoids the problems introduced by polar angles that are too small or too large.

Next, the effect of possible misalignments on the estimate of the state was studied. Each of the three LIDAR beams can have misalignments in one or both of two directions. These misalignments are in the polar angle of 22.5° from vertical, and in their clock angle separation of 120° from one another. Additionally, misalignments were also incorporated into the entire beam head assembly. For this study, maximum errors of ± 2° in any direction were considered the maximum expected alignment error. The study was therefore conducted using the maximum possible misalignment magnitudes in each direction at once. That is, all LIDAR pointing direction errors and head assembly pointer errors were ± 2° at the same time. The results of the study are shown in Fig. 4.

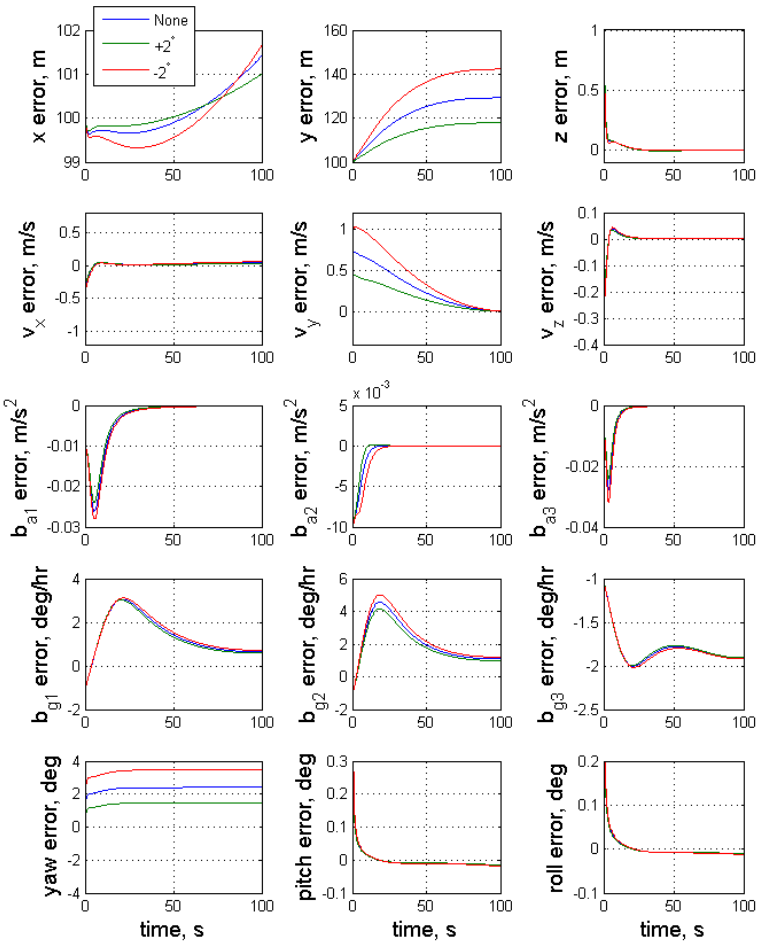

Fig. 4 Errors in estimated state for beam and head assembly misalignments

As would be expected, misalignments introduce errors into the estimated states. The trend can be seen in all plots that misalignment in one direction causes a certain shift in the estimate, while the opposite misalignment creates an opposite shift. In the x and y position estimates, the shift is not symmetric, due to the fact that x and y are not well defined for a flat surface. Thus, minute errors in the velocity estimate tend to accumulate in the position estimates. However, even with the maximum possible misalignment errors occurring at the same time, the overall effect of the misalignments is minimal. Estimates of the velocity and accelerometer and gyro biases are slightly slower to return to the true state, but the magnitude of the error is nearly the same as without misalignments. While other studies with misalignments up to 10° showed significant errors in the estimated states, misalignments of that magnitude are unlikely in this system. Misalignments on the order of 2° as in this study would not be likely to cause any significant errors in the estimated spacecraft state during application.

Finally, the influence of limited data types was studied. Simulations were run in which only range or only Doppler measurements were used. This was conducted to simulate errors in the data collection which may occur during operations. To accomplish this, the uncertainty of the measurements was drastically increased (by 15 orders of magnitude), such that the measurements have no effect on the estimate of state. The same trajectory was used, with the standard polar angle of 22.5°. Fig. 5 details the state estimate errors for these simulations.

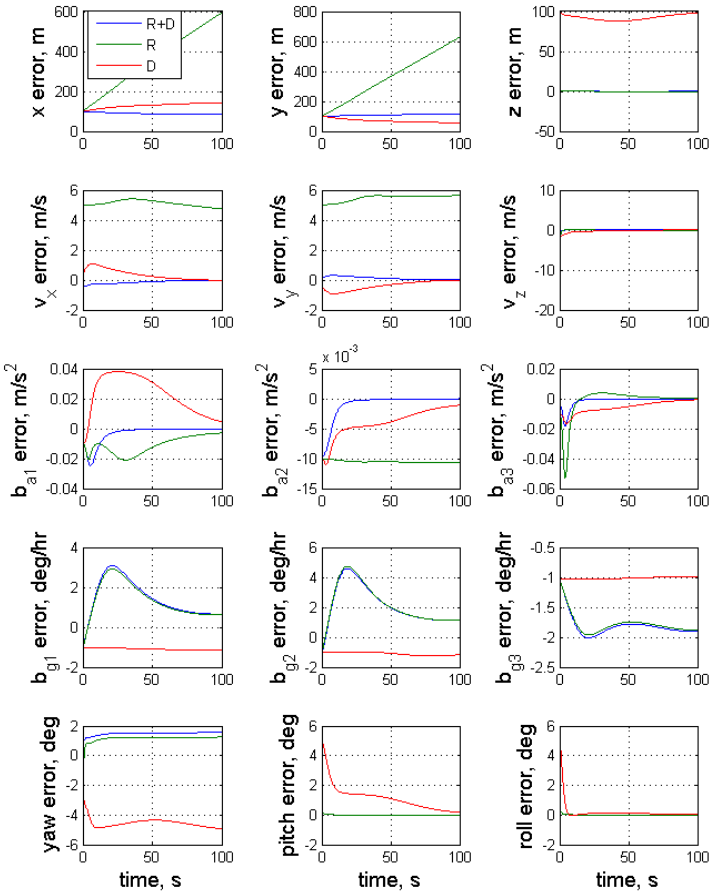

Fig. 5 Errors in estimated state for limited data types

The results of the study indicate that, as expected, having measurements of both range and Doppler provides the best estimate of the state as opposed to having only one type. For the range only case, the altitude and vertical velocity are well determined, as is orientation. However, all other estimated states suffer significantly. For the Doppler only case, velocities are better estimated than with range. This is expected, as the Doppler measures line of sight velocity, which feeds into the estimate of the spacecraft velocity. However, altitude, orientation, and biases cannot be well estimated with Doppler only. This shows that range measurements provide better estimates of geometrically-determined quantities such as altitude and orientation, while Doppler measurements provide better estimates of velocity. The inclusion of both data types provides the advantages of both, leading to the best possible estimate of the spacecraft state.

B. Rocky Terrain

A rocky terrain simulation was generated using hemispherical bumps. A flat plane was described, and hemispheres with a normally distributed diameter were randomly placed on the plane. For the following results, an average bump size of 3 meters was used. The trajectory is identical to that presented in the previous section. Fig. 6 shows the sample terrain including bumps, and the LIDAR beam ground tracks.

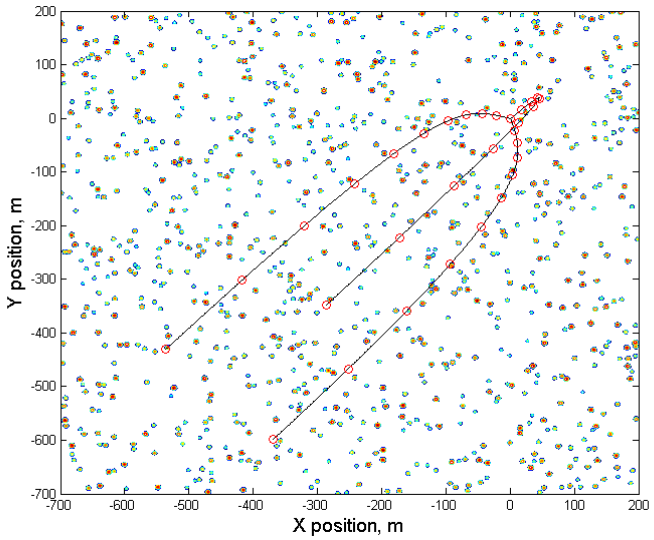

Fig. 6 Simulated bumpy terrain and LIDAR ground tracks

Initial simulation showed that the original tuning of the filter produced significant errors in the estimated states. Multiple methods to account for the errors introduced by the terrain were explored. One method was an intervention method, comparing each range measurement to the measurement at the previous time. If the change between the two is beyond a certain threshold, that measurement would not be used. However, the option that was selected was to a simple retuning of the filter parameters. This would reduce the errors introduced by the terrain, but still use the original filter without changing the approach. The retuned quantities included modifying the measurement uncertainties and state noise, among others.

Fig. 7 shows a few selected states for the trajectory over bumpy terrain, including both the original filter and the retuned filter results. For the original filter tuning, large errors in x and y location (hundreds of meters) are introduced due to the terrain. These states cannot be estimated for a flat surface, so any errors that are introduced cannot be corrected. The reason for the large deviation in x position becomes clear in the plot below, showing the x velocity estimate. The x velocity has error on the order of 10 m/s due to the influence of the terrain. This error is primarily due to the errors in estimated orientation, which cause the Doppler measurements to feed into the velocity estimate differently. The estimated velocity does return to the true state, but very slowly. The errors in estimated velocity feed into the position estimate, so the larger the error in velocity, the faster the error in position will grow.

The primary driver in reducing the errors introduced by the terrain is inflating the uncertainty of the range measurements. While the LIDAR system is accurate to 1 centimeter or less, increasing the uncertainty to a level approximately the same as the bump size (2-5 meters) decreases the error introduced by terrain. Note that the errors in all estimated states are reduced with the retuned filter. This retuned filter was then adopted in further simulations.

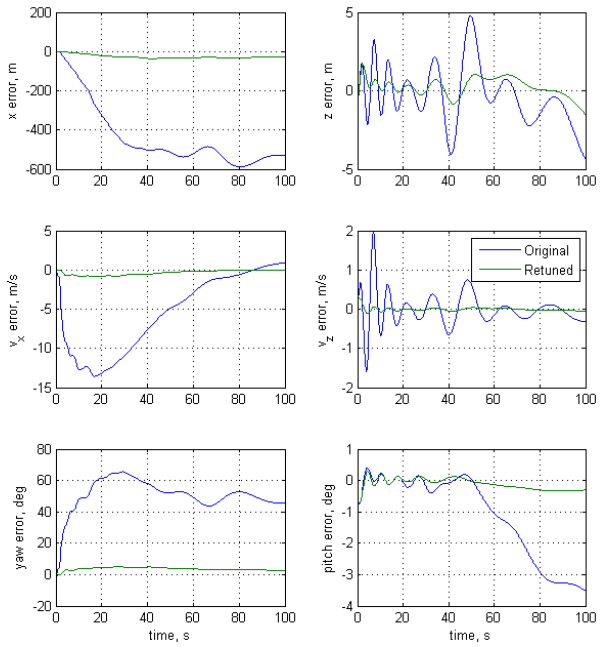

Fig. 7 Select errors in estimated state for 3 meter radius rocky terrain

C. Hilly Terrain

Another terrain used in simulation testing was a hilly terrain (or "washboard"). The height of the terrain varies with x according to $\sin(2\pi x/\lambda)$, where λ is the wavelength of the terrain. At each x, the height is constant for all y. A sample terrain is presented in Fig. 8. The effect of the hilly terrain on the estimated state was analyzed by flying in the x-direction at a constant altitude and velocity. Over a long enough trajectory, the errors in the estimated states approach the steady state solution and become periodic. Fig. 9 shows selected states for a trajectory at a constant velocity and altitude of 1 m/s and 350 m, respectively. The spacecraft travels over a washboard surface with height 5 m and wavelength 100 m.

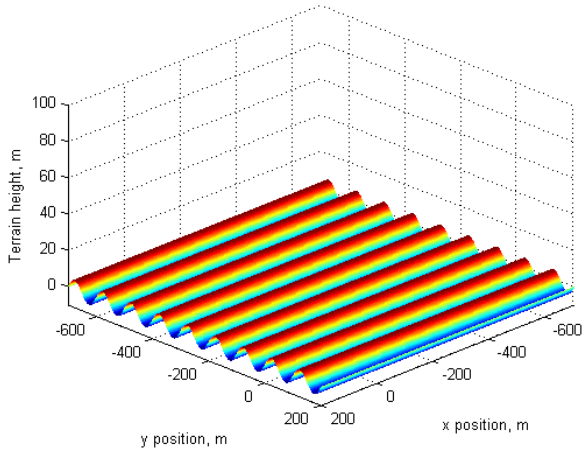

Fig. 8 Sample washboard terrain, 5m amplitude by 100m wavelength

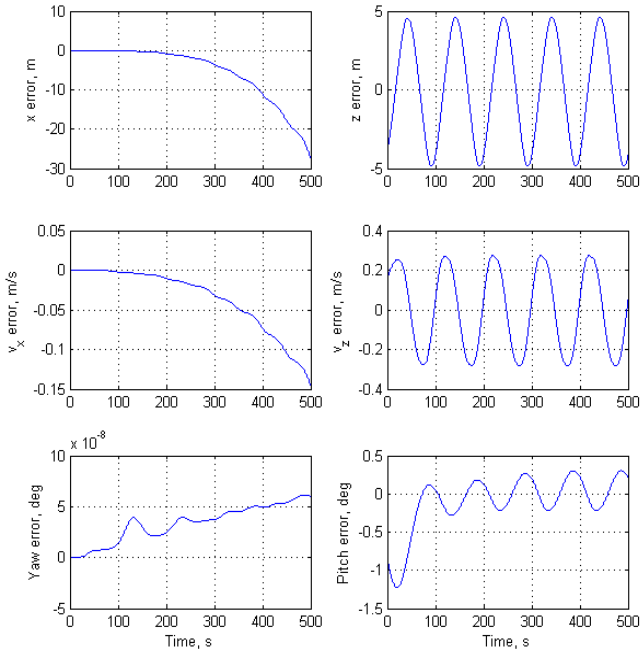

Fig. 9 Select errors in estimated state for 5m x 100m washboard

By studying the response of the filter to various washboards and trajectories, it became clear that the amplitude of the error in the estimated state is essentially determined by the "apparent" frequency that the LIDAR beam detects. That is, the frequency of changes in the LIDAR observations due to the terrain, defined as v_{sc} / λ, where v_{sc} is the spacecraft's velocity. By testing various values of this apparent frequency and examining the amplitude of the state errors, a gain bode plot can be constructed. Fig. 10 shows a Bode plot for the spacecraft's altitude for several values of frequency. It can be seen that the height of the terrain does not have a large impact on the altitude gain. Whether the terrain height is 1, 5, or 10 m, the gain is approximately the same. This linear result may not hold at all altitudes or very large terrain amplitudes.

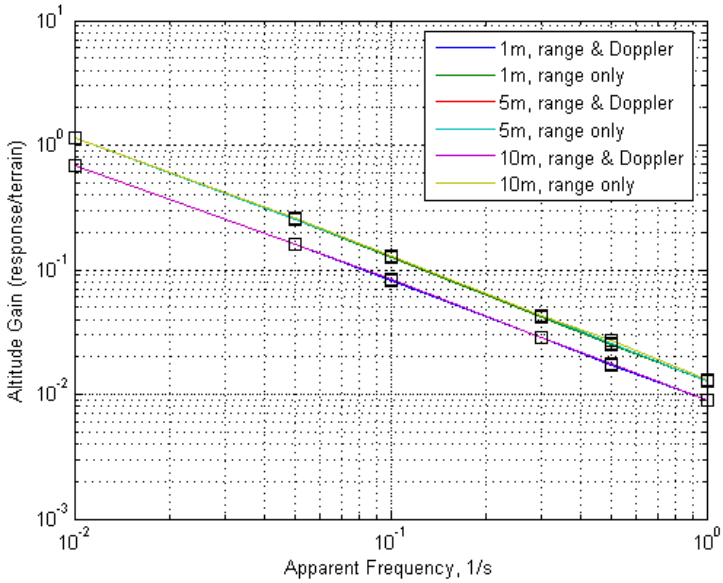

Fig. 10 Altitude gain vs. apparent frequency for 100m wavelength terrains at 300m altitude

Next, the effect of the spacecraft altitude on the altitude gain was studied. Over the same range of apparent frequencies, the altitude of the spacecraft was varied between 200 and 400 meters. The results of simulations are shown in Fig. 11, below.

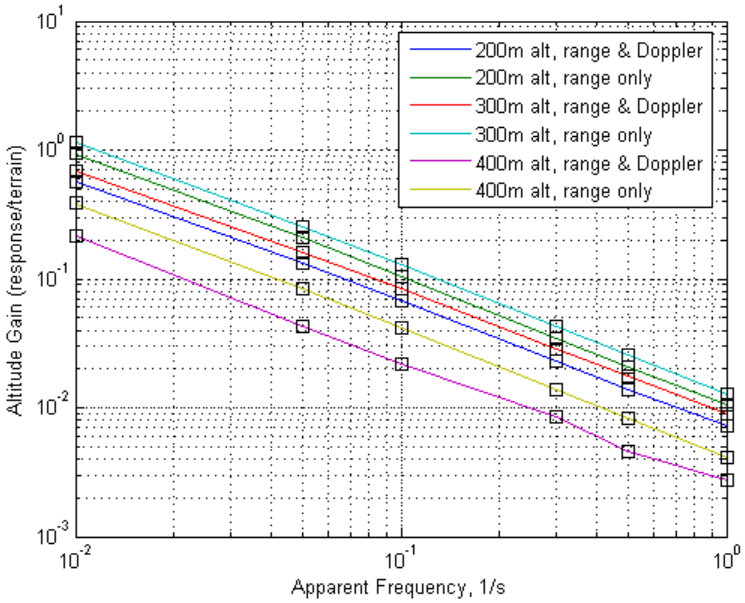

Fig. 11 Effect of spacecraft altitude on altitude gain, 5m x 100m terrain

The same pattern of decreasing gain with increasing frequency is again evident, as is the shift in the curves due to the inclusion or exclusion of Doppler measurements. Because the Doppler measurements affect the position estimate through velocity, the "range only" gains will always be larger than the corresponding case including Doppler measurements. There is also a clear effect of the spacecraft altitude on the gain. Changes in the altitude result in effective upward or downward shifts of the gain curve. Note that increasing the spacecraft altitude from 200 to 300m increases the gain, while increasing from 300 to 400m decreases it. This seemingly contradictory result is due to the geometry of the LIDAR beams and terrain. A main factor in this phenomenon is the phase difference between the forward (1) and rear (2 & 3) LIDAR beams. The spacecraft altitude and footprint in the x-direction can be described through the following relation: $ftprnt = (alt)\sin(a)(1-\cos(\mu))$. For a given trajectory, the footprint was varied between and 45 and 720 degrees. For a 360 degree width footprint, the footprint is the same length as the terrain wavelength, and scales linearly. To accomplish this, the altitude was varied according to the above relation. Fig. 12 shows the resulting altitude gain.

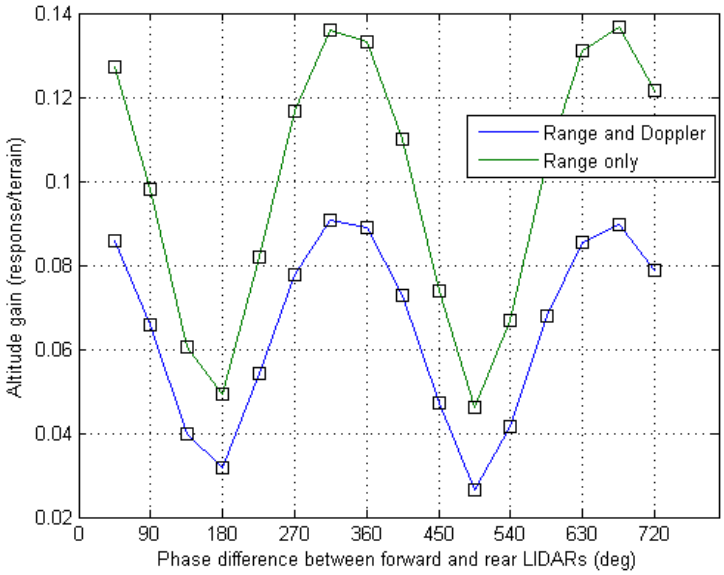

Fig. 12 Effect of LIDAR phase difference on altitude gain, 1m x 100m terrain, 10 m/s

The altitude gain, rather than steadily increasing or decreasing with increasing altitude, fluctuates according to the phase difference between the forward and rear LIDAR beams. The gain follows a similar pattern whether the Doppler measurements are included with the range measurements or not. Again, in the range only case, the altitude gain is larger. That is, the estimated altitude changes a greater amount, due to the decrease in available information caused by the lack of Doppler measurements. Note that the minimum gain occurs at 180 degrees, while the maximum occurs at 360 degrees. The reason for the shift that causes the minimum and maximum not to occur at 540 and 720 degrees is lag caused by the geometry of the beams and the increased altitude.

V. Experimental Results

A LIDAR system developed at NASA Langley Research Center was installed aboard a Eurocopter AS350D helicopter and tested in a series of six flights over the California desert near NASA Dryden from August 20-22, 2008. This section presents the results from analysis of the second flight test, which occurred over a flat, dry lake bed.

A. Experiment Description

The LIDAR was mounted on the nose of the helicopter inside a gimbaled spherical shroud, which was designed to point nadir throughout the flight. Unfortunately, due to problems with the gimbal control software, nadir-lock was not maintained when the helicopter turned. LIDAR measurements of range and Doppler velocity were taken at the rate of 10 Hz. In addition, a LN-200 Inertial Measurement Unit was mounted along with the LIDAR inside of the shroud at the front of the helicopter. IMU measurements were sampled at the rate of 400 Hz. The helicopter was also equipped with an onboard GPS sensor. Uncertainties in GPS measurements are typically small—on the order of 1 cm and 1 cm/s for position and velocity, respectively—and thus GPS-measured position and velocity closely approximate the actual state of the helicopter. Total flight time was roughly one half-hour.

The origin of the navigation frame was at the point on the surface below the initial position of the helicopter, as measured along the local vertical. The *z*-axis is coincident with the local geodetic vertical; the *x*- and *y*-axes are directed toward north and west, respectively. The navigation frame is planet-fixed and rotates with the Earth.

The origin of the vehicle body coordinate system is taken to be the IMU center of mass. The *x*-axis (roll axis) points forward along the longitudinal axis of the vehicle. The *y*-axis (pitch axis) is directed 90 degrees to the left when facing forward, normal to the roll axis. The *z*-axis (yaw axis) is directed upward normal to the *xy*-plane.

Including only the central term, gravitational acceleration was calculated at the initial position of the helicopter. For simplicity, gravity was held at this constant value throughout the navigation.

B. Discussion

A 2.5 minute interval near the beginning of the flight was selected for analysis. The Kalman filter routine was run with and without LIDAR measurements to estimate the state of the helicopter over time. In both cases, initial estimates for position, velocity, and attitude were set equal to the corresponding reference initial conditions. To facilitate physical interpretation of the results, the attitude is presented as yaw, pitch, and roll angles rather than the four element quaternion. Here, it should be noted that the true state of the vehicle is obviously unknowable. GPS measurements were taken to represent the reference position and velocity, while the reference attitude was taken to be the Euler angle data provided by the ALHAT team at Jet Propulsion Laboratory. The details and quality of that attitude analysis, including error estimates, were not available as of this writing.

The Kalman filter was tuned by trial and error to minimize the residuals, defined as the difference between the actual and estimated values. The results can be viewed in the following figures: the upper row in each figure shows residuals resulting from IMU-only integration, while the lower row contains plots of residuals for the case that LIDAR observations are used to correct the state estimate. Position and velocity residual components are plotted in the navigation frame.

Note that the accelerometer bias cannot be estimated without LIDAR observations. Because the bias changes very slowly in time, the error in this parameter is nearly constant. Likewise, error in the gravity model is also nearly constant since gravitational acceleration cannot be expected to vary significantly from one time or location to the next. The combination of these constant errors in acceleration yields linear errors in velocity and quadratic errors in position, which can be seen in the upper rows of Fig. 13 and Fig. 14. This is not true for the *y*-component, though, possibly because the two errors in this direction are negligible or partially cancel one another.

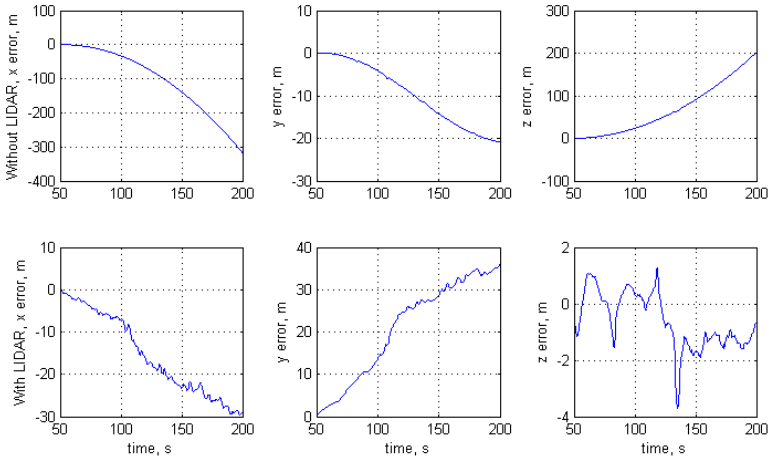

Fig. 13 Position error versus time without (top row) and with (bottom row) LIDAR measurements

LIDAR observations, however, mitigate much of the error associated with the uncertainties in the gravity model and accelerometer bias. As seen in Fig. 6, by the end of the 2.5 minute period, the LIDAR has reduced the error in the *x*-component of position by an order of magnitude when compared to the IMU-only case. Error in altitude is two orders of magnitude less than that in the case of exclusive IMU integration. Doppler velocity measurements update all three components of the velocity vector, which has the effect of improving the position estimates. The estimate in *z* is best, however, since range measurements only update this component of position in the case of a flat surface. In addition, the LIDAR geometry is most favorable for estimating the *z*-component of velocity for level flight.

The effect of the LIDAR observations on the velocity estimate is shown in the bottom row of Fig. 14. Residuals in this case are on the order of 0.1 m/s, an order of magnitude less than the residuals at the 200 s mark without the LIDAR.

Here, it should be noted that because gravity and specific force appear as part of an algebraic sum in the equations of motion, errors in these two terms are indistinguishable to the Kalman filter. Accordingly, the part of the measurement residual which is actually due to the gravity model error is mistakenly assigned by the filter to accelerometer bias. This phenomenon is known as aliasing. The simple gravity model used here certainly differs from the actual gravity field, and thus the gravity model error has been aliased into the estimated accelerometer bias.

Because the gyro bias is nearly constant, errors in the Euler angles (Fig. 15) should be linearly increasing in the case of IMU-only integration. For the short 2.5 minute period under investigation, the attitude estimates without

LIDAR are quite good since the gyro bias is so small. Over long time periods, however, even slight gyro drift would cause substantial attitude errors. Assuming a flat surface, the LIDAR measurements only update the pitch and roll estimates; residuals for these two angles are on the order of 0.1 deg. Yaw is not updated, as expected for the case of a flat landing surface. The LIDAR measurements prevent the pitch and roll estimates from drifting but also introduce fairly significant noise, possibly due to local terrain undulations or misalignment of the LIDAR beams.

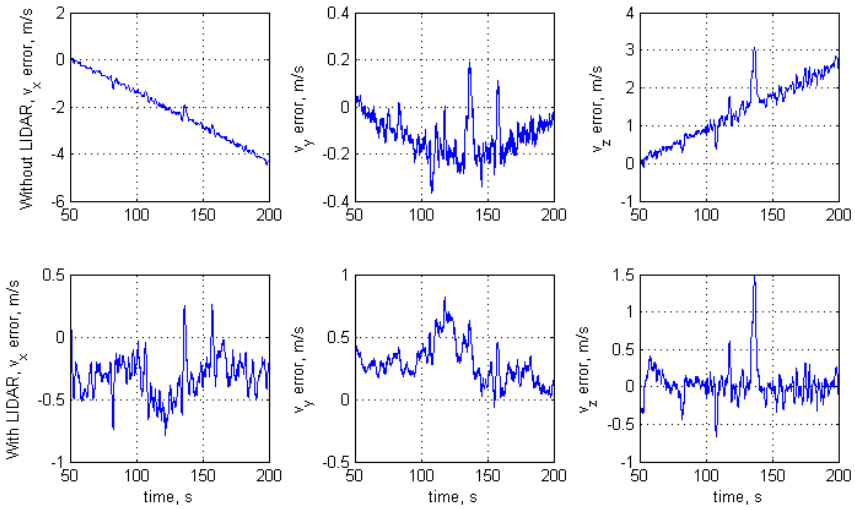

Fig. 14 Velocity error versus time without (top row) and with (bottom row) LIDAR measurements

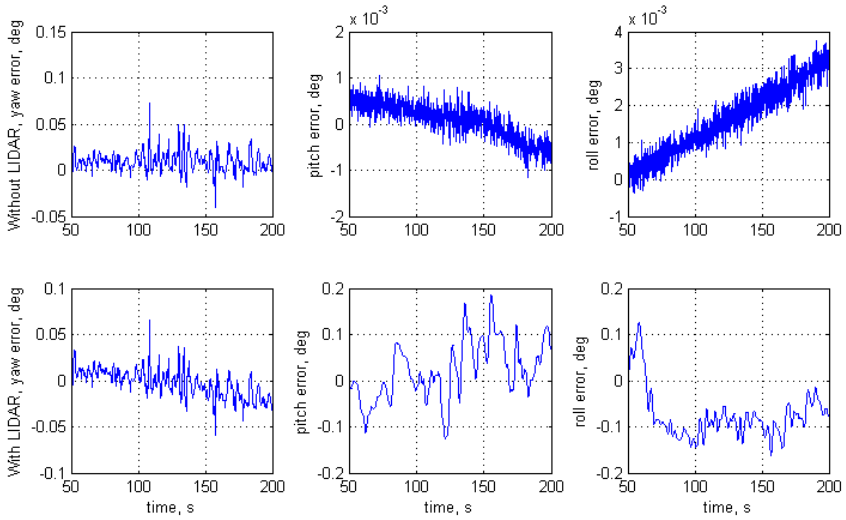

Fig. 15 Attitude error versus time without (top row) and with (bottom row) LIDAR measurements

VI. Conclusion

An algorithm for accurately estimating spacecraft position, velocity, and attitude during landing has been presented. The proposed estimator combines IMU-measured acceleration and angular velocity with LIDAR range and Doppler velocity measurements in an extended Kalman filter framework to significantly enhance state estimation. Overall, filter results from a helicopter flight test are in excellent agreement with GPS data. Of particular

note is that the new LIDAR system is orders of magnitude more accurate than existing flight-proven navigation systems that rely exclusively on IMU measurements.

Lessons garnered from the studies presented here will prove to be valuable in the processing of flight test data, from another round of tests conducted in 2010. As of this writing, data from these tests is being processed, but is not yet in a usable state. In addition, demonstration of this new pinpoint landing technology has direct relevance to future space missions, including Lunar South Pole/Aitken Basin Sample Return, Comet/Asteroid Surface Sample Return, Venus In-Situ Explorer, Mars Sample Return, Europa Lander, Titan Explorer, as well as human exploration missions to the Moon and Mars.

Research presented in this document was conducted in partial fulfillment of the degrees of Master of Science for both Matthew Aitken and David Busnardo from North Carolina State University.

References

[1] Striepe, S.A., Epp. C.D., and Robertson, E.A., "Autonomous Precision Landing and Hazard Avoidance Technology (ALHAT) Project Status as of May 2010," International Planetary Probe Workshop Proceedings, Paper 457, 2010.

[2] Amzajerdian, F., Pierrottet, D., Tolson, R.H., Powell, R.W., Davidson, J.B., and Peri, F., "Development of a Coherent LIDAR for Aiding Precision Soft Landing on Planetary Bodies," Proc. of 13th Coherent Laser Radar Conference, Kamakura, Japan, October 16-20, 2005.

[3] Pierrottet, D., Amzajerdian, F., Petway, L., Barnes, B., and Lockard, G., "Flight test performance of a high precision navigation Doppler LIDAR," Proc. SPIE 7323, 732311, 2009.

[4] Farrenkopf, R.L., "Analytic Steady-State Accuracy Solutions for Two Common Spacecraft Attitude Estimators," *Journal of Guidance and Control*, Vol. 1, No. 4, 1978, pp. 282-284.

[5] Lefferts, E.J., Markley, F.L., and Shuster, M.D., "Kalman Filtering for Spacecraft Attitude Estimation," *Journal of Guidance, Control, and Dynamics*, Vol. 5, No. 5, 1982, pp. 417-429.

[6] Trawny, N., Mourikis, A.I., Roumeliotis, S.I., Johnson, A.E., and Montgomery, J.F., "Vision-Aided Inertial Navigation for Pin-Point Landing using Observations of Mapped Landmarks," *Journal of Field Robotics*, Vol. 24, No. 5, 2007, pp. 357-378.

[7] Meirovitch, L., *Methods of Analytical Dynamics*, McGraw-Hill, New York, 1970.